energies

MDPI

Article

Holistic Dynamic Modeling and Simulation of Alkaline Water Electrolysis Systems Based on Heat Current Method

Yi-Chong Jiang [1], Shi-Meng Dong [2], Zheng Liang [1], Xiao-Li Wang [3], Lei Shi [3], Bing Yan [3] and Tian Zhao [1,*]

[1] Department of Engineering Mechanics, Tsinghua University, Beijing 100084, China; 13188071337@163.com (Y.-C.J.); liangz20@mails.tsinghua.edu.cn (Z.L.)
[2] National Power Dispatch and Control Center, State Grid Corporation of China, Xicheng District, Beijing 100031, China; dong-shimeng@sgcc.com.cn
[3] State Grid Ningxia Electric Power Co., Ltd., Yinchuan 750000, China; wangxiaoli@nx.sgcc.com.cn (X.-L.W.); shilei@nx.sgcc.con.cn (L.S.); yanbing@nx.sgcc.com.cn (B.Y.)
* Correspondence: gszhaotian@126.com

Abstract: Hydrogen production technology is becoming increasingly important with the rapid development of hydrogen energy. Among existing hydrogen production technologies, alkaline water electrolysis (AWE) is drawing wide attention due to its advantages such as high maturity and low cost, and its performance analysis and optimization are important for applications. However, the AWE system contains processes with different physical and mathematical properties such as electrochemical reaction and heat transport processes, bringing difficulties to the system modeling. Moreover, the electrical and thermal processes have different characteristic time scales, and the system shows a sophisticated dynamic behavior, which has not been well studied yet. Here, a homomorphic dynamic model of the AWE system in the form of electrical circuit is built to describe the thermal and electrochemical processes uniformly, where the two parts are integrated via the energy conservation seamlessly. The model is verified by comparing with the experimental data and shows a high accuracy. The dynamic simulation analysis is conducted to investigate the dynamic response characteristics of the system under current step changes and fluctuations. The temperature overshoot and oscillation phenomena caused by delays in heat transport processes are studied. Results show that the time delay yields a maximum temperature overshoot of 10 °C, which would reduce the lifespan of the stack. This also highlights the importance of dynamic system analysis.

Keywords: alkaline water electrolysis; dynamic modeling; heat current method; equivalent circuit; multi-time scales

check for updates

Citation: Jiang, Y.-C.; Dong, S.-M.; Liang, Z.; Wang, X.-L.; Shi, L.; Yan, B.; Zhao, T. Holistic Dynamic Modeling and Simulation of Alkaline Water Electrolysis Systems Based on Heat Current Method. *Energies* **2024**, *17*, 6202. https://doi.org/10.3390/en17236202

Academic Editor: Eugenio Meloni

Received: 9 November 2024
Revised: 4 December 2024
Accepted: 4 December 2024
Published: 9 December 2024

Copyright: © 2024 by the authors. Licensee MDPI, Basel, Switzerland. This article is an open access article distributed under the terms and conditions of the Creative Commons Attribution (CC BY) license (https://creativecommons.org/licenses/by/4.0/).

1. Introduction

Hydrogen energy, as a clean and efficient secondary energy source, plays an important role in promoting the energy transition and addressing the climate change [1–3]. Electrolytic hydrogen production plays a crucial role in energy storage and peak shaving within an integrated energy system. By utilizing surplus electricity from renewable sources like wind and solar power, it converts excess energy into hydrogen, which not only improves energy utilization but also reduces the burden on traditional power dispatch systems. However, the intermittent and fluctuating nature of wind and solar power poses challenges to the operational stability of water electrolysis. At the same time, the electrolysis process itself involves complex electrochemical reactions and energy transport, which significantly influence the system's dynamic characteristics and overall efficiency [4]. Alkaline water electrolysis (AWE) technology has attracted considerable attention in industrial-scale hydrogen production due to its technological maturity and low-cost advantages compared to anion exchange membrane electrolysis (AEM) [5], proton exchange membrane electrolysis (PEM), and solid oxide electrolysis cell (SOEC). AWE technology remains a key focus for its practicality and economic benefits. [6,7]. Therefore, establishing the accurate dynamic

model for AWE is crucial for understanding and optimizing the hydrogen production process driven by renewable energy [8,9].

The dynamic modeling of AWE has been extensively studied, and both three-dimensional (3D) mechanism models and reduced order models have been developed. Jaeseung et al. [10] established a 3D transient model for AWE systems based on conservation equations and chemical reaction models, elucidating the electrochemical reactions and transport phenomena in the water electrolysis process. However, the calculation is complex as the model takes the form of differential equations, which also makes it challenging to couple with power electronic devices for the controlling. Besides, the heat transfer process is ignored, resulting the difficulty in thermal management. Ulleberg et al. [11] proposed a dynamic model of AWE consisting of both electrochemical and thermal parts and has been widely used. However, the voltage calculation relies on an empirical formula of temperature solely, and the electrochemical model could not describe the effects of electrolyte concentration and bubbles on overpotential. Jang et al. [12] analyzed the effect of pressure on AWE system performance through numerical simulations based on an electrochemical mechanism model, but did not consider the heat transfer inside. Sakas et al. [13] proposed a dynamic mass and energy balance simulation model for AWE devices, based on a semi-empirical electrochemical model and a lumped heat transfer model. Ding et al. [14] established an energy flow model for a 250 kW AWE system and conducted studies on cold starts, based on an electrochemical mechanism model and a lumped heat transfer model. Qi et al. [9] developed a thermal management model for an alkaline electrolysis system under dynamic operating conditions based on an empirical electrochemical model and a lumped thermal model and designed its controller. These models are based on the lumped-parameter heat transfer models, which inevitably causing errors in analysis. Besides, they would also introduce intermediate variables, increasing the complexity of system simulation. Moreover, they mainly focus on the dynamic behavior at the minute scale and above but fail to resolve the multi-time scale characteristics of the AWE system.

The equivalent circuit method is another approach to analyze and simulate AWE systems. In this approach, the AWE is modeled in the form of electrical circuit, which can be seamlessly integrated with the power system model, benefiting the holistic analysis of integrated energy systems. Ursúa et al. [15] developed an equivalent circuit model for the AWE operating at steady-state. The model considers the polarization phenomena during electrolysis but did not take the heat transfer into account, failing to fully consider the system's thermal characteristics. Therefore, this method has not been well applied in the dynamic modeling of the AWE system where the thermal characteristics are crucial.

Recently, Chen et al. [16] proposed the heat current method following the philosophy of thermal-electrical analogy. It models thermal systems in the form of electrical circuits by introducing the concept of thermal resistance of heat exchangers [17]. It eliminates unnecessary intermediate variables and thus simplifying the system simulation. Besides, the heat current model can be integrated with the electrochemical mechanism model seamlessly to construct the system's overall equivalent circuit model, benefiting the integration with power electronic devices. This method has been widely applied in the thermal and integrated power and thermal systems. For instance, Xin et al. [18] utilized the heat current method to optimize the operation of multiple CHP units with flexibility retrofits for the real-time coordination of power and heat generation to improve energy efficiency. He et al. [19] employed the heat current method to study the optimal operation of an integrated power and thermal system to improve the wind power accommodation. In addition to conventional energy systems, the heat current method has also been extended to the field of electrochemical systems. Hao et al. [20] established analyzed the impact of heat transfer process on the overall performance of a SOFC cogeneration system by combining an equivalent circuit model of internal electrochemical process and a heat current model of the external heat exchanger. Liang et al. [21] proposed a multi-energy circuit model of a SOFC consisting of both electrical and thermal circuits, which improves the analysis efficiency substantially.

This paper constructs a holistic dynamic model of the AWE system that fully describes the energy conversion and transport processes inside. The electrochemical part is modeled by using the equivalent circuit model, and the thermal part is modeled by using the heat current method. Based on the system model, the dynamic characteristics of the AWE system is analyzed. Besides, the model accounts for heat transport delays and heat leakage of components, making the model more accurate. Furthermore, this work analyses the system's multi-time scale characteristics also provides the key response characteristics such as power output and hydrogen production rates tailored to different time scales.

The rest of this paper is organized as follows. In Section 2, the AWE system modeling process is introduced in detail. The solution algorithm of the model is proposed in Section 3, and the model is also validated by comparing against both experimental and numerical results from existing studies. In Section 4, the dynamic behavior as well as the performance of the AWE system is studied in depth. Major conclusions are summarized in Section 5.

2. Holistic Modeling of the AWE System

2.1. Structure and Working Principle of the AWE System

The AWE system considered in this work mainly consists of a stack, two gas-liquid separators for hydrogen and oxygen, an electrolyte pump, a heat exchanger, and a water tank, as Figure 1 shows [14]. It also includes additional purification devices and electrical systems, which are not included here. In the AWE system operation, the electrochemical reaction occurs in the electrolyte of the stack driven by the direct electrical current. On the cathode side, water molecules in the electrolyte gain electrons and undergo a hydrogen evolution reduction reaction, producing hydrogen gas and OH^- ions. The OH^- ions pass through the membrane due to the concentration difference between the cathode and anode sides, as well as the effect of the electric field. On the anode side, OH^- ions lose electrons and undergo an oxygen evolution oxidation reaction, producing oxygen gas and water. The mixture of hydrogen gas/electrolyte and oxygen gas/electrolyte generated by the reaction flows out of the stack and enters two separators, respectively. The gases leave the system, while the electrolyte returns to the mixer for remixing. The electrolyte flowing out of the mixer is first pressurized by the pump, then cooled by the cooling water in a heat exchanger to maintain the temperature of the stack. Finally, a PID controller uses the average temperature of the stack as the temperature set point [9]. By adjusting the opening of the cooling water valve, it regulates the cooling water flow to keep the stack temperature near the set point.

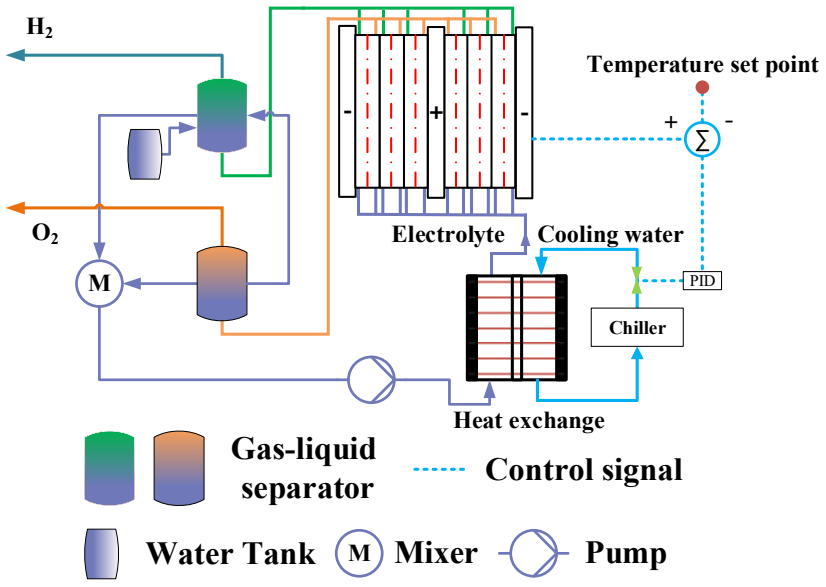


Figure 1. Sketch of the AWE system.

Following assumptions are adopted in the modeling process:

1. Due to the short characteristic time constants, the electrochemical reactions and the variations of mass flow rates of electrolytes in the stack are regarded as instantaneous and analyzed by using steady-state models [15].
2. The stack temperature is assumed to be uniform and equal to the average temperature of the inlet and outlet. Besides, the amount of replenished water is equal to the ideal amount consumed by the chemical reaction, thereby maintaining a constant electrolyte mass flow for safety [9].
3. In the modeling of gas-liquid separators, the mixer, and the pipeline, gases are considered ideal gases, the gas and liquid are completely separated in separators, the temperature variation of gases during separation and that of electrolyte during the compression are negligible, and the specific heat capacity of water replenished or consumed is assumed to be equal to that of the electrolyte [14].
4. In the dynamic modeling of the heat exchanger, the fluid flow is considered as one-dimensional, the physical properties of the fluid are regarded as constant, the heat exchanger has no heat leakage, and the heat conduction of the fluid and the heat exchange wall in the direction of fluid flow is ignored. The inlet temperature of the cold fluid is assumed to be the ambient temperature in the calculation [22].

2.2. Electrochemical Model of the AWE System

The stack is composed of multiple electrolytic cells connected in series and parallel. The cell voltage U_{cell} of the stack is the sum of the reversible voltage U_{rev}, the ohmic overpotential U_{ohm} due to internal resistance, the activation overpotential U_{act} due to kinetic limitations of the anode and cathode reactions, and the concentration overpotential U_{con} due to concentration differences. U_{con} is usually negligible at higher current densities [23], and hence yields:

$$U_{\text{cell}} = U_{\text{rev}} + U_{\text{act,c}} + U_{\text{act,a}} + U_{\text{ohm}} \tag{1}$$

2.2.1. Reversible Voltage

The reversible voltage is the minimum voltage required for a chemical reaction and is influenced by temperature, pressure, and activity of the water. In non-standard conditions, it is calculated by the Nernst equation [24]:

$$U_{\text{rev}} = U^0_{\text{rev}} + \frac{RT}{2F} \ln\left[\frac{\left(P - P_{\text{H}_2\text{O}}\right)^{1.5}}{\alpha_{\text{H}_2\text{O}}}\right] \tag{2}$$

where U^0_{rev} is the standard reversible voltage, which is a function of temperature T, R is the gas constant, F is Faraday's constant, P is the operating pressure, and $P_{\text{H}_2\text{O}}$ is the water vapor partial pressure, expressed by empirical formulas related to alkali concentration m, stack average temperature T, $\alpha_{\text{H}_2\text{O}}$ indicates water activity in the range of 0–150 °C [14]. It is noted that all temperatures used in this paper are in Kelvin.

$$U^0_{\text{rev}} = 1.50342 - 9.956 \times 10^{-4} T + 2.5 \times 10^{-7} T^2 \tag{3}$$

$$\begin{aligned} \log P_{\text{H}_2\text{O}} &= -0.01508m - 0.0016788m^2 + 2.25887 \times 10^{-5} m^3 \\ &+ \left(1 - 0.0012062m + 5.6024 \times 10^{-4} m^2 - 7.8228\right. \\ &\left. \times 10^{-6} m^3\right) \times (35.4462 - 3343.93/T - 10.9 \log T \\ &+ 0.004165T) \end{aligned} \tag{4}$$

$$\begin{aligned} \log \alpha_{\text{H}_2\text{O}}(\text{KOH}) &= -0.02255m + 0.001434m^2 \\ &+ \left(1.38m - 0.9254m^2\right)/T \end{aligned} \tag{5}$$

where the molar concentration m can be calculated from the mass fraction concentration w [12]:

$$m = \frac{w}{56.105}\left(\begin{array}{c} 183.1221 - 0.56845T \\ +984.5679\exp\left(\frac{w}{1.1596277}\right) \end{array} \right) \quad (6)$$

2.2.2. Activation Overpotential

The activation overpotential is related to the activation energy of electrochemical reactions and represents the voltage needed to break the equilibrium and drive the electrochemical reaction. Considering the influence of bubbles on the exchange current density, the activation overpotentials at two sides, $U_{\text{act,c}}$ and $U_{\text{act,a}}$ are calculated as [24]:

$$U_{\text{act,c}} = \frac{RT}{2\alpha_{\text{c}}F}\ln\left[\frac{J}{J_{0,\text{c}}(1-\theta)}\right] \quad (7)$$

$$U_{\text{act,a}} = \frac{RT}{2\alpha_{\text{a}}F}\ln\left[\frac{J}{J_{0,\text{a}}(1-\theta)}\right] \quad (8)$$

where J is the current density, $J_{0,\text{a}}$ and $J_{0,\text{c}}$ represent the exchange current densities of the anode and cathode, θ is the ratio of electrode surface covered by generated bubbles, and α is the transfer coefficient of the electrodes. In this work, the stack uses nickel electrodes, and the parameters are calculated following [12], respectively:

$$J_{0,\text{a}} = 0.9\left(\frac{P}{P_0}\right)^{0.1}\exp\left[-\frac{42000}{RT}\left(1-\frac{T}{T_0}\right)\right] \quad (9)$$

$$J_{0,\text{c}} = 1.5\left(\frac{P}{P_0}\right)^{0.1}\exp\left[-\frac{23000}{RT}\left(1-\frac{T}{T_0}\right)\right] \quad (10)$$

$$\theta = \left[-97.25 + 182\frac{T}{T_0} - 84\left(\frac{T}{T_0}\right)^2\right]\left(\frac{J}{J_{\text{lim}}}\right)^{0.3}\frac{P}{P - P_{\text{H}_2\text{O}}(T)} \quad (11)$$

$$\alpha_{\text{a}} = 0.07835 + 0.001T \quad (12)$$

$$\alpha_{\text{c}} = 0.1175 + 0.00095T \quad (13)$$

where P is the operating pressure, T_{ref} is the reference temperature, and P_{ref} is the reference pressure. J_{lim} is the limiting current density under 100% bubble coverage, with a typical value of 300 kA m^{-2}, which is not the real current density on the electrodes [25].

2.2.3. Ohmic Overpotential

The total ohmic overpotential U_{ohm} in the stack is the voltage drop caused by the resistance of the electrolyte to the flow of current. It is calculated from the resistance R^*_{ohm}, which consists of resistances of anode R^*_{a}, cathode R^*_{c}, electrolyte $R^*_{\text{KOH-bubble}}$, and membrane R^*_{mem} [12]:

$$U_{\text{ohm}} = R^*_{\text{ohm}}I = (R^*_{\text{c}} + R^*_{\text{a}} + R^*_{\text{KOH-bubble}} + R^*_{\text{mem}}) \times I \quad (14)$$

$$R^*_{\text{a}} = \frac{1}{\sigma_{\text{a}}}\left(\frac{\delta_{\text{a}}}{S_{\text{a}}}\right),\ R^*_{\text{c}} = \frac{1}{\sigma_{\text{c}}}\left(\frac{\delta_{\text{c}}}{S_{\text{c}}}\right) \quad (15)$$

where I is the current, and δ_{a}, δ_{c}, S_{a}, and S_{c} are the thickness and area of the anode and cathode, respectively. σ_{a} and σ_{c} represent the conductivity of the anode and cathode. They are equal to the electrical conductivity of Nickel σ_{Ni} and is the function of temperature:

$$\sigma_{\text{a}} = \sigma_{\text{c}} = \sigma_{\text{Ni}} = 60000000 - 279650T + 532T^2 - 0.38057T^3 \quad (16)$$

The resistance of electrolyte considering the effect of bubbles inside $R_{\text{KOH-bubble}}$ is determined by the original resistance of electrolyte R^*_{ele} and the correction term of bubbles. R^*_{ele} is calculated as [12]:

$$R^*_{\text{ele}} = \frac{1}{\sigma_{\text{KOH}}}\left(\frac{d_{\text{am}}}{S_{\text{a}}} + \frac{d_{\text{cm}}}{S_{\text{c}}}\right) \tag{17}$$

where d_{am} and d_{cm} are the distances between the anode and cathode to the membrane, respectively. σ_{KOH} is the electrolyte conductivity and is related to the concentration and temperature of the electrolyte:

$$\sigma_{\text{KOH}} = a_0 m + a_1 mT + a_2 mT^{-1} + a_3 m^2 + a_4 m^3 + a_5 m^2 T^2 \tag{18}$$

where coefficients a_0–a_5 are given in Table 1 [26].

Table 1. Coefficients for calculating σ_{KOH}.

a_0	a_1	a_2	a_3	a_4	a_5
−2.041	5.332×10^{-3}	2.072×10^{2}	-2.8×10^{-3}	1.043×10^{-3}	-3×10^{-7}

Bubbles generate and transport in the electrolyte during electrolysis, and they reduce the electrolyte's conductivity. This effect can be corrected by using the Bruggeman Equation [27]:

$$\sigma_{\text{KOH-bubble}} = \left(1 - \frac{2}{3}\theta\right)^{\frac{3}{2}} \sigma_{\text{KOH}} \tag{19}$$

Consequently, the electrolyte resistance considering the effect of bubbles is calculated as:

$$R^*_{\text{KOH-bubble}} = R^*_{\text{ele}}\left(1 - \frac{2}{3}\theta\right)^{-\frac{3}{2}} \tag{20}$$

Membrane resistance R^*_{mem} depends on the porosity, tortuosity and cross-sectional area of the membrane as well as the electrolyte conductivity. For the non-organic Zirfon-based membrane use in the stack, R^*_{mem} is determined as [14,28]:

$$R^*_{\text{mem}} = \frac{\delta_{\text{m}} \tau_{\text{m}}}{p_{\text{m}} \sigma_{\text{KOH}} S_{\text{m}}} \tag{21}$$

where δ_{m} is the membrane thickness, p_{m} is the membrane porosity, τ_{m} represents the tortuosity of the transverse membrane, and S_{m} is the cross-sectional area of the transverse membrane.

Assembling all overpotentials gives the electrical circuit model of a single cell in the AWE shown in Figure 2, which describes the electrochemical processes inside. The model of the entire stack is further obtained by connecting multiple cell models.

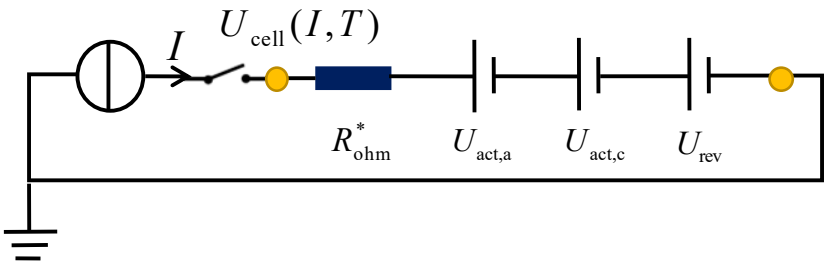


Figure 2. Electrical circuit model of a cell in the stack.

2.3. Heat Current Model of the AWE System

2.3.1. Heat Current Model of the Stack

The energy conservation analysis of the stack is first conducted, and the heat balance relation of the stack is given in Figure 3. The stack has an inner heat source caused by the electrolysis process. Meanwhile, it also releases heat to the environment due to the temperature difference. Finally, the enthalpy flows carried by the electrolyte flows into and out from the stack are also to be considered.

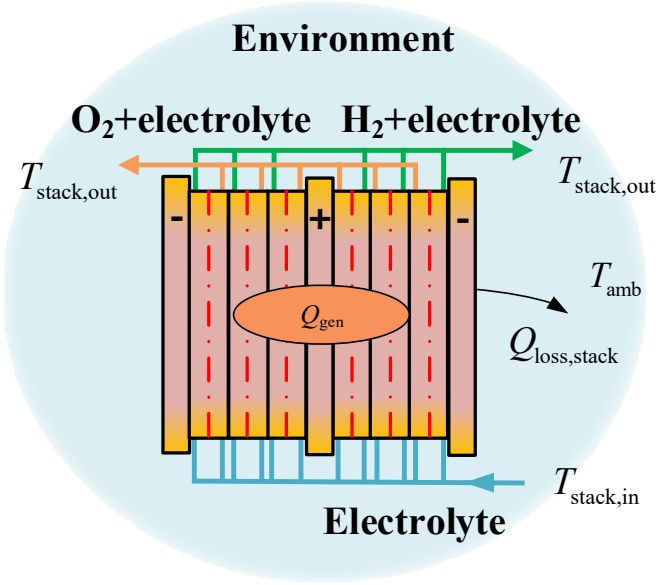


Figure 3. Heat balance diagram of the stack.

(1) The electrolysis process generates heat as the voltage exceeds the thermal neutral voltage. The heat generation rate Q_{gen} of the stack is [9]:

$$Q_{\text{gen}}(t) = N(U_{\text{cell}}(t) - U_{\text{th}})I(t) \tag{22}$$

where N is the number of electrolysis chambers, U_{cell} is the cell voltage, and U_{th} is the thermal neutral voltage with the value of 1.48 V [9].

(2) The stack also releases heat to the environment, and this process is described by using a thermal resistance R_{stack} in the heat current method [29]:

$$R_{\text{stack}}(t) = \frac{T_{\text{stack}}(t) - T_{\text{amb}}}{Q_{\text{loss,stack}}(t)} = \frac{1}{KA_{\text{stack}}} \tag{23}$$

where KA_{stack} represents the thermal conductance of heat loss between the stack and the environment, and T_{amb} is the ambient temperature. The stack temperature T_{stack} is regarded as the average of inlet and outlet temperature of stack [9]:

$$T_{\text{stack}}(t) = \frac{T_{\text{stack,out}}(t) + T_{\text{stack,in}}(t)}{2} \tag{24}$$

(3) The temperature of the electrolyte flows through the stack rises due to the internal heat source Q_{gen}. In the heat current method, this temperature rise can be described by using a thermo-motive force ε_{gen} [29]:

$$\varepsilon_{\text{gen}}(t) = T_{\text{stack,out}*}(t) - T_{\text{stack,in}}(t) = \frac{Q_{\text{gen}}(t) - Q_{\text{loss,stack}}(t)}{\dot{m}_{\text{lye}}c_{\text{lye}}} \tag{25}$$

where t marks the time, and $\dot{m}_{\mathrm{lye}}$ and c_{lye} denote the mass flow rate and specific heat capacity of the electrolyte, respectively. $T_{\mathrm{stack,out}*}(t)$ denotes the outlet temperature of the electrolyte element that flows in the stack at time t, as Figure 4 shows.

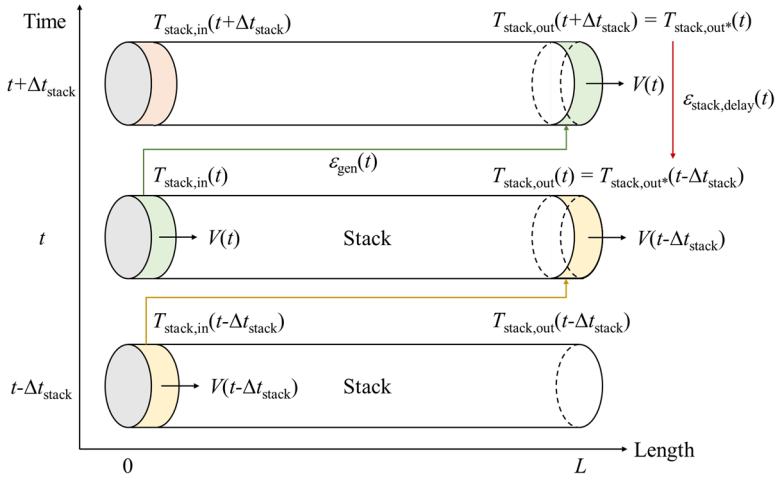


Figure 4. Sketch of the heat transport process in the stack, the stack is simplified as a pipeline for clarity.

Meanwhile, due to the limited flow speed of the electrolyte, the heat transport process in the stack also has a time delay. This delay effect can be considered by using an additional thermo-motive force [30]:

$$\varepsilon_{\mathrm{stack,delay}}(t) = T_{\mathrm{stack,out}*}(t) - T_{\mathrm{stack,out}*}(t - \Delta t_{\mathrm{stack}}) \tag{26}$$

where $\varepsilon_{\mathrm{stack,delay}}$ represents the delay effect caused by the heat transport process within the stack, and $\Delta t_{\mathrm{stack}}$ is the delay time within the stack. $\Delta t_{\mathrm{stack}}$ is determined by dividing the volume of the flow channel in the stack by the volumetric flow rate of the electrolyte [9]. Time delay is unavoidable; however, increasing the electrolyte flow rate can reduce the delay. Nonetheless, it is essential to balance this with the system's design requirements and practical operating conditions. Figure 4 gives a graphical explanation of this calculation. Finally, combining Equations (25) and (26) gives the stack outlet temperature $T_{\mathrm{stack,out}}$ at time t:

$$T_{\mathrm{stack,out}}(t) = T_{\mathrm{stack,out}*}(t) - \varepsilon_{\mathrm{stack,delay}}(t) \tag{27}$$

(4) The temperature of the stack may vary in the dynamic operation process, as it has the heat capacity of C_{stack}. In the heat current model, the heat capacity can be described by using a thermal capacitance.

After obtaining the models of all components, connecting them referring to the energy flow topology gives the heat current model of the stack, as Figure 5 shows. The model shows that the temperature of the stack T_{stack} varies depending on the heat taken away by the electrolyte, the heat produced by the stack, and the heat loss with the environment.

The overall constraint equation of the stack concerning each boundary temperature can be obtained by applying the Kirchhoff's voltage law (KVL).

$$C_{\mathrm{stack}} \frac{\mathrm{d}T_{\mathrm{stack}}(t)}{\mathrm{d}t} = \dot{m}_{\mathrm{lye}} c_{\mathrm{lye}} \left(\varepsilon_{\mathrm{stack,delay}}(t) - \varepsilon_{\mathrm{gen}}(t) \right) + Q_{\mathrm{gen}}(t) - Q_{\mathrm{loss,stack}}(t) \tag{28}$$

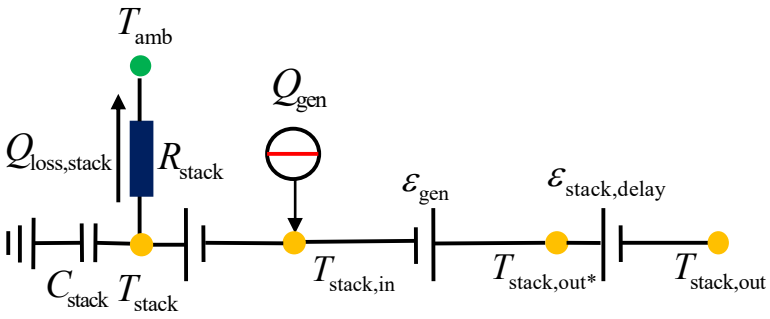


Figure 5. Heat current model of the stack.

2.3.2. Heat Current Model of Other Components

Hydrogen gas-liquid separator and the pipes. In the hydrogen gas-liquid separator, the supply water and a part of the water on the oxygen side mix, and it releases heat to the environment at the same time. Similar to the stack, Figure 6 presents its heat balance relation.

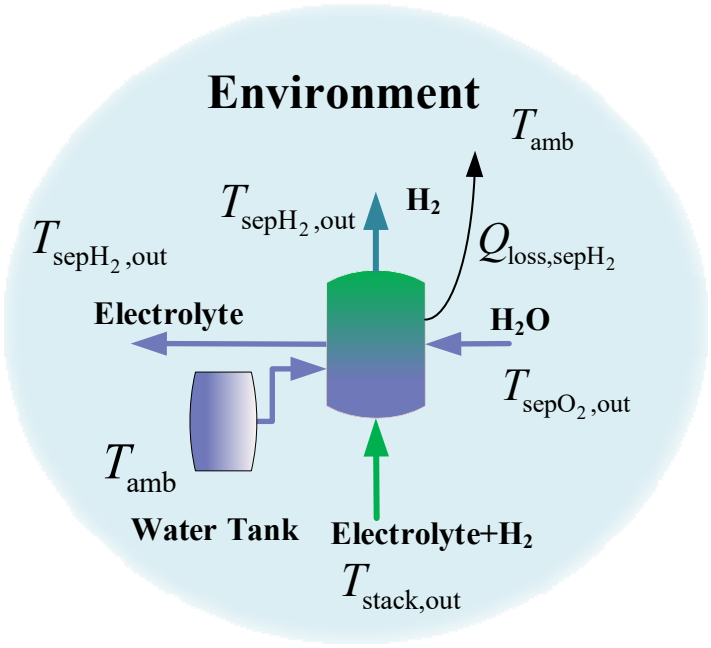


Figure 6. Heat balance of the hydrogen gas-liquid separator.

Similar to the stack model, $\varepsilon_{loss,sepH_2}$ is used to represent the thermo-motive force for the fluid mixing and heat loss in the hydrogen gas separator [29]:

$$\varepsilon_{loss,sepH_2}(t) = T_{sepH_2,out*}(t) - T_{stack,out}(t) \tag{29}$$

where $T_{sepH_2,out*}$ is the temperature after the mixed materials entering the hydrogen gas separator are mixed and dissipate heat with the environment:

$$T_{sepH_2,out*}(t) = \frac{\sum H - Q_{loss,sepH_2}(t)}{0.5\dot{m}_{lye}c_{lye} + \dot{m}_{H_2}c_{H_2}} \tag{30}$$

$$\begin{aligned}\sum H \quad &= \left(0.5\dot{m}_{lye} - 2\dot{m}_{H_2O}\right)c_{lye}T_{stack,out}(t) + \dot{m}_{H_2O}c_{lye}T_{sepO_2,out}(t) + \dot{m}_{H_2O}c_{lye}T_{amb}(t) \\ &+\dot{m}_{H_2}c_{H_2}T_{stack,out}(t)\end{aligned} \tag{31}$$

where $Q_{loss,sepH_2}$ is the heat releases to the environment, $2\dot{m}_{H_2O}$, $\dot{m}_{H_2}$, $\dot{m}_{lye}$ are the mass flow rate of water consumed for hydrogen gas production, the mass flow rate of hydrogen

gas production, the mass flow rate of electrolyte, respectively. c_{lye}, $c_{\mathrm{H_2}}$ are the specific heat capacities of electrolyte and hydrogen gas, respectively.

The heat release process between the separator and the environment follows [29]:

$$R_{\mathrm{sepH_2}}(t) = \frac{T_{\mathrm{sepH_2}}(t) - T_{\mathrm{amb}}}{Q_{\mathrm{loss,sepH_2}}(t)} = \frac{1}{KA_{\mathrm{sep}}} \tag{32}$$

where $R_{\mathrm{sepH_2}}$ is the thermal resistance of heat loss between the hydrogen gas separator and the environment, and KA_{sep} is the thermal conductance of heat release between the gas-liquid separator and the environment.

The delay of heat transport in the gas-liquid separator can be calculated using the volume of the liquid phase in the separator and the electrolyte flow rate. The corresponding thermo-motive force is:

$$\varepsilon_{\mathrm{delay,sepH_2}}(t) = T_{\mathrm{sepH_2,out*}}(t) - T_{\mathrm{sepH_2,out*}}(t - \Delta t_{\mathrm{sep}}) \tag{33}$$

$$T_{\mathrm{sepH_2,out}}(t) = T_{\mathrm{sepH_2,out*}}(t) - \varepsilon_{\mathrm{delay,sepH_2}}(t) \tag{34}$$

where $\varepsilon_{\mathrm{sepH_2,delay}}$ represents the delay effect caused by the heat transport process within the separator, and Δt_{sep} is the delay time within the separator. Similar to above, Δt_{sep} can be calculated by dividing the liquid phase volume in the gas-liquid separator by the volumetric flow rate of the electrolyte entering the gas-liquid separator. The liquid level of the gas-liquid separator is calculated with reference to half of the height of the gas-liquid separator. $T_{\mathrm{sepH_2,out}}$ is the temperature at the outlet of the hydrogen separator at the current moment and $T_{\mathrm{sepH_2,out}}$ is the temperature before the time shift.

The temperature of the hydrogen gas-liquid separator $T_{\mathrm{sepH_2}}$ is calculated as [9]:

$$T_{\mathrm{sepH_2}}(t) = \frac{T_{\mathrm{stack,out}}(t) + T_{\mathrm{sepH_2,out}}(t)}{2} \tag{35}$$

The overall constraint equation of the hydrogen gas-liquid separator concerning each boundary temperature can be obtained by applying Kirchhoff's voltage law (KVL).

$$\frac{C_{\mathrm{sepH_2}}\mathrm{d}T_{\mathrm{sepH_2}}(t)}{\mathrm{d}t} = \left(0.5\dot{m}_{\mathrm{lye}}c_{\mathrm{lye}} + \dot{m}_{\mathrm{H_2}}c_{\mathrm{H_2}}\right)\left(\varepsilon_{\mathrm{delay,sepH_2}}(t) - \varepsilon_{\mathrm{loss,sepH_2}}(t)\right) \tag{36}$$

For the pipeline connected to the hydrogen separator, the heat leakage and delay should be considered simultaneously. Here the ambient temperature T_{amb} is spatially uniform and only varies with time. The heat leakage thermal resistance of the pipeline is expressed as [30]:

$$R_{\mathrm{pipeH_2}} = \frac{2}{(1 - \exp(-b_p))m_{\mathrm{lye}}c_{\mathrm{lye}}} \tag{37}$$

where $R_{\mathrm{pipeH_2}}$ represents the heat transfer resistance reflecting the heat leakage characteristics of the piping on the hydrogen gas separator side, and $b_{\mathrm{p}} = \tau_{\mathrm{flow}}/\tau_{\mathrm{loss}}$ reflects the relative importance between the overall heat transfer characteristics of the pipeline and the heat transfer characteristics [30].

$$\tau_{\mathrm{flow}} = \frac{L_{\mathrm{pipe}}}{V_{\mathrm{lye}}} \tag{38}$$

$$\tau_{\mathrm{loss}} = \frac{\rho_{\mathrm{lye}}c_{\mathrm{lye}}s_{\mathrm{pipe}}}{K_{\mathrm{pipe}}B_{\mathrm{pipe}}} \tag{39}$$

where V_{lye} is the volume flow of electrolytic liquid, L_{pipe} is the length of the pipe, s_{pipe} is the cross-sectional area of the pipe, K_{pipe} is the heat transfer coefficient between the fluid and the environment, and B_{pipe} is the perimeter of the pipe.

The temperature variation of lye and heat release rate between the pipeline and the environment are [29]:

$$\varepsilon_{\text{loss,H}_2\text{pipe}} = \frac{2Q_{\text{loss,pipeH}_2}}{m_{\text{lye}}c_{\text{lye}}} \tag{40}$$

$$Q_{\text{loss,pipeH}_2} = \frac{T_{\text{sepH}_2,\text{out}} - T_{\text{amb}}}{R_{\text{pipeH}_2}} \tag{41}$$

Finally, an additional thermo-motive force is introduced to shift the outlet temperature time to the temperature at the current moment [30]:

$$\varepsilon_{\text{delay,pipeH}_2} = T_{\text{C,mix}*}(t) - T_{\text{C,mix}*}(t - \tau_{\text{flow}}) \tag{42}$$

$$T_{\text{C,mix}*}(t) = T_{\text{sepH}_2,\text{out}}(t) - \varepsilon_{\text{loss,pipeH}_2}(t) \tag{43}$$

$$T_{\text{C,mix}}(t) = T_{\text{C,mix}*}(t) - \varepsilon_{\text{delay,pipeH}_2}(t) \tag{44}$$

where $\varepsilon_{\text{delay,pipeH}_2}$ is the delayed thermo-motive force during heat transport in the pipeline, $T_{\text{C,mix}}$ is the temperature at the current moment, and $T_{\text{C,mix}*}$ is the temperature before the time shift.

Finally, connecting these components together gives the heat current model of the hydrogen gas-liquid separator, as Figure 7 shows.

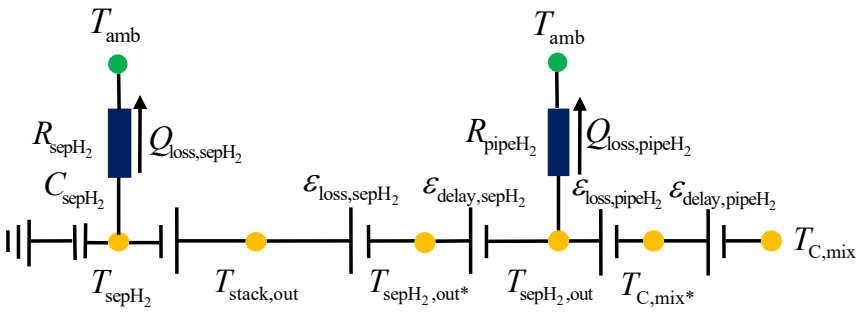


Figure 7. Heat current model of the hydrogen gas-liquid separator and the pipeline.

Oxygen gas-liquid separator and the pipes. The oxygen gas-liquid separator is similar to the hydrogen gas-liquid separator, and its heat balance relation is given in Figure 8. The thermal resistance R_{sepO_2} and thermo-motive force $\varepsilon_{\text{loss,sepO}_2}$ representing the heat transfer between the oxygen gas separator and the environment are [29]:

$$R_{\text{sepO}_2}(t) = \frac{T_{\text{sepO}_2}(t) - T_{\text{amb}}}{Q_{\text{loss,sepO}_2}(t)} = \frac{1}{KA_{\text{sep}}} \tag{45}$$

$$\varepsilon_{\text{loss,sepO}_2}(t) = T_{\text{stack,out}}(t) - T_{\text{sepO}_2,\text{out}*}(t) = \frac{Q_{\text{loss,sepO}_2}(t)}{0.5\dot{m}_{\text{lye}}c_{\text{lye}} + \dot{m}_{\text{O}_2}c_{\text{O}_2} + \dot{m}_{\text{H}_2\text{O}}c_{\text{lye}}} \tag{46}$$

Similar to the above, the delayed thermo-motive force of oxygen gas separator is:

$$\varepsilon_{\text{delay,sepO}_2}(t) = T_{\text{sepO}_2,\text{out}*}(t) - T_{\text{sepO}_2,\text{out}*}(t - \Delta t_{\text{sep}}) \tag{47}$$

$$T_{\text{sepO}_2,\text{out}}(t) = T_{\text{sepO}_2,\text{out}*}(t) - \varepsilon_{\text{delay,sepO}_2}(t) \tag{48}$$

where $T_{\text{sepO}_2,\text{out}}$ is the temperature at the outlet of the hydrogen separator at the current moment, and $T_{\text{sepO}_2,\text{out}}$ is the temperature before the time shift.

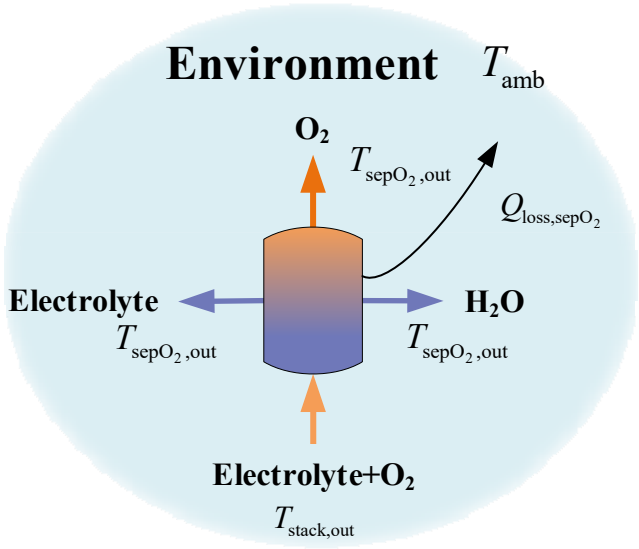


Figure 8. Heat balance of the oxygen gas-liquid separator.

The temperature of the oxygen gas-liquid separator is calculated as [9]:

$$T_{\mathrm{sepO_2}}(t) = \frac{T_{\mathrm{stack,out}}(t) + T_{\mathrm{sepO_2,out}}(t)}{2} \tag{49}$$

The overall constraint equations of the oxygen gas-liquid separator concerning each boundary temperature can be obtained by applying Kirchhoff's voltage law (KVL).

$$\frac{C_{\mathrm{sepO_2}} dT_{\mathrm{sepO_2}}(t)}{dt} = \left(0.5\dot{m}_{\mathrm{lye}} c_{\mathrm{lye}} + \dot{m}_{\mathrm{O_2}} c_{\mathrm{O_2}} + \dot{m}_{\mathrm{H_2O}} c_{\mathrm{lye}}\right)\left(\varepsilon_{\mathrm{delay,sepO_2}}(t) + \varepsilon_{\mathrm{loss,sepO_2}}(t)\right) - Q_{\mathrm{loss,sepO_2}}(t) \tag{50}$$

where KA_{sep} is the thermal conductance of heat transfer process between the gas-liquid separator and the environment, $Q_{\mathrm{loss,sepO_2}}$ is the heat leakage rate, $\varepsilon_{\mathrm{delay,sepO_2}}$ represents the delay effect caused by the heat transport process within the separator, and Δt_{sep} is the delay time within the separator.

The heat leakage of the pipe connected to the oxygen gas-liquid separator, and the delay in the heat transport is calculated in the same way as on the hydrogen side. The entire process is described by using a thermal resistance and a thermo-motive force, and they are calculated as [30]:

$$R_{\mathrm{pipeO_2}}(t) = \frac{2}{(1 - \exp(-b_p))\, m_{\mathrm{lye}} c_{\mathrm{lye}}} \tag{51}$$

$$\varepsilon_{\mathrm{loss,pipeO_2}}(t) = \frac{2Q_{\mathrm{loss,pipeO_2}}(t)}{m_{\mathrm{lye}} c_{\mathrm{lye}}} \tag{52}$$

$$Q_{\mathrm{loss,pipeO_2}}(t) = \frac{T_{\mathrm{sepO_2,out}}(t) - T_{\mathrm{amb}}}{R_{\mathrm{pipeO_2}}(t)} \tag{53}$$

where $R_{\mathrm{pipeO_2}}$ is the thermal resistance describing the heat leakage between the pipeline on the oxygen gas separator side and the environment, b_{p} is the same as that on the hydrogen gas separator side, $Q_{\mathrm{loss,pipeO_2}}$ is the heat release rate of the pipeline, and $\varepsilon_{\mathrm{loss,pipeO_2}}$ describes the temperature variation of the fluid in the pipeline. Furthermore, a thermo-motive force $\varepsilon_{\mathrm{delay,pipeO_2}}$ describing the time translation is used to describe the delay of the heat transport in the pipeline [22,31]:

$$\varepsilon_{\mathrm{delay,pipeO_2}}(t) = T_{\mathrm{A,mix*}}(t) - T_{\mathrm{A,mix*}}(t - \tau_{\mathrm{flow}}) \tag{54}$$

$$T_{\mathrm{A,mix}*}(t) = T_{\mathrm{sepO_2,out}}(t) - \varepsilon_{\mathrm{loss,pipeO_2}}(t) \tag{55}$$

$$T_{\mathrm{A,mix}}(t) = T_{\mathrm{A,mix}*}(t) - \varepsilon_{\mathrm{delay,pipeO_2}}(t) \tag{56}$$

where $T_{\mathrm{A,mix}}$ is the temperature at the current moment, and $T_{\mathrm{A,mix}^*}$ is the temperature before the time shift.

Connecting all these components gives the heat current model of the oxygen gas-liquid separator, as Figure 9 shows.

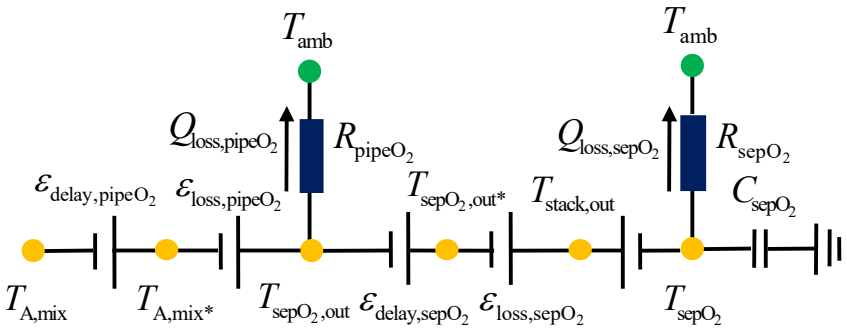


Figure 9. Heat current model of the oxygen gas-liquid separator and the pipeline.

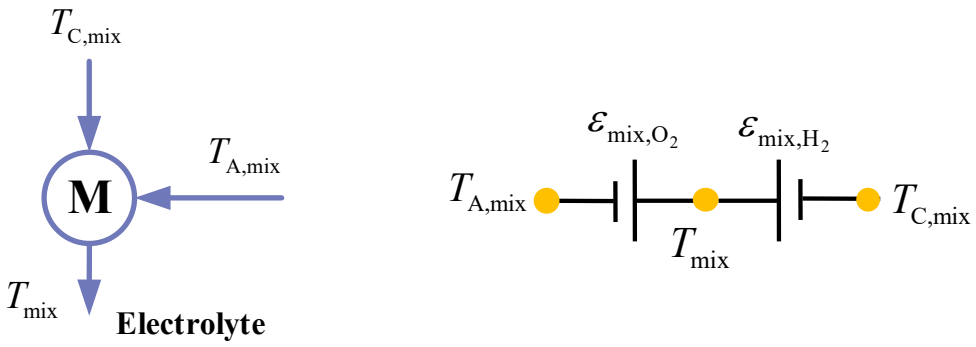
Mixer. The electrolytes on the hydrogen side and oxygen side enter the mixer and merge, as Figure 10a shows. The mixing process finishes immediately, and the mass flow rates of two streams of electrolyte are the same, yielding [22]:

$$T_{\mathrm{mix}}(t) = \frac{T_{\mathrm{C,mix}}(t) + T_{\mathrm{A,mix}}(t)}{2} \tag{57}$$

where $T_{\mathrm{C,mix}}$, $T_{\mathrm{A,mix}}$, and T_{mix} represent the outlet temperatures of the pipelines on the hydrogen gas separator side, the oxygen gas separator side, and the temperature after mixing of the two electrolytes, respectively. In heat current method, this process can be described by using two thermo-motive forces, $\varepsilon_{\mathrm{mixH_2}}$ and $\varepsilon_{\mathrm{mixO_2}}$, to reflect the temperature variations of the electrolyte on both sides [29], as Figure 10b presents.

$$\varepsilon_{\mathrm{mix,H_2}}(t) = T_{\mathrm{mix}}(t) - T_{\mathrm{C,mix}}(t) = \frac{T_{\mathrm{C,mix}}(t) + T_{\mathrm{A,mix}}(t)}{2} - T_{\mathrm{C,mix}}(t) \tag{58}$$

$$\varepsilon_{\mathrm{mix,O_2}}(t) = T_{\mathrm{mix}}(t) - T_{\mathrm{A,mix}}(t) = \frac{T_{\mathrm{C,mix}}(t) + T_{\mathrm{A,mix}}(t)}{2} - T_{\mathrm{A,mix}}(t) \tag{59}$$



(**a**) (**b**)

Figure 10. Mixer model, (**a**) schematic diagram of the mixer, (**b**) heat current model of the mixer.

Heat Exchanger. The dynamic heat current model of the heat exchanger can be developed by combining its steady-state model and the heat storage and migration characteristics

inside [16]. For the heat exchanger shown in Figure 11a, its heat current model is given as Figure 11b. The two thermal resistances $R_{ex,h}$ and $R_{ex,c}$ represent the heat transfer processes between hot/cold fluid and the wall, respectively:

$$Q_h(t) = \frac{T_{mix}(t) - T_w(t)}{R_{ex,h}} \tag{60}$$

$$Q_c(t) = \frac{T_w(t) - T_{c,in}(t)}{R_{ex,c}} \tag{61}$$

where Q_h and Q_c are the heat transfer rates between the two fluids and wall, respectively. $R_{ex,h}$ and $R_{ex,c}$ are defined as [22].

$$R_{ex,h} = 1/\left[G_h\left(1 - \exp\left(-\frac{KA_h}{G_h}\right)\right)\right] \tag{62}$$

$$R_{ex,c} = 1/\left[G_c\left(1 - \exp\left(-\frac{KA_c}{G_c}\right)\right)\right] \tag{63}$$

where G represents the heat capacity flow of the fluid, namely the product of mass flow rate $\dot{m}$ and specific heat capacity c_p:

$$G_c = \dot{m}_c c_{p,c}, G_h = \dot{m}_{lye} c_{p,lye} \tag{64}$$

where KA_h and KA_c represent the product of the overall heat transfer coefficients and the heat transfer area at the hot and cold ends of the heat exchanger, respectively.

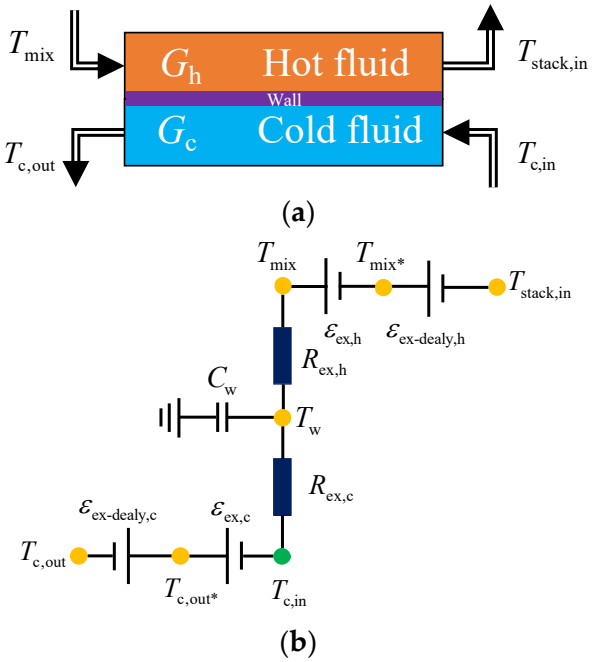


Figure 11. Dynamic heat current model of heat exchanger, (**a**) schematic diagram of the heat exchanger, (**b**) heat current model of the heat exchanger.

The energy conservation of the wall gives [22]:

$$C_w \frac{dT_w(t)}{dt} = Q_h - Q_c \tag{65}$$

where C_w is the heat capacity of the wall.

Similar to the pipelines in the gas-liquid separator, the outlet temperatures of hot and cold fluids, $T_{\text{stack,in}}$ and $T_{\text{c,out}}$, can be obtained by considering the energy conservation and the delay effect of heat transport process [22]:

$$T_{\text{stack,in}}(t) = T_{\text{mix}}(t) - \varepsilon_{\text{h}}(t) - \varepsilon_{\text{h,delay}}(t) \tag{66}$$

$$T_{\text{c,out}}(t) = T_{\text{c,in}}(t) + \varepsilon_{\text{c}}(t) - \varepsilon_{\text{c,delay}}(t) \tag{67}$$

$$\varepsilon_{\text{ex-delay,h}}(t) = T_{\text{mix}*}(t) - T_{\text{mix}*}(t - \Delta t_{\text{ex,h}}) \tag{68}$$

$$\varepsilon_{\text{ex-delay,c}}(t) = T_{\text{c,out}*}(t) - T_{\text{c,out}*}(t - \Delta t_{\text{ex,c}}) \tag{69}$$

where $\varepsilon_{\text{ex-delay,h}}$ and $\varepsilon_{\text{ex-delay,c}}$ represent the delay effect caused by the heat migration process of hot and cold fluids. $\Delta t_{\text{ex,h}}$ and $\Delta t_{\text{ex,c}}$ are the delay time and are determined by dividing the volume of the flow channel by the volumetric flow rate of the corresponding fluid. ε_{h} and ε_{c} are thermo-motive forces that reflects the temperature variations of two fluids due to the energy conservation.

Similarly, connecting all models above referring to the temperature nodes gives the heat current model of the heat exchanger, as Figure 11b shows.

To further improve the modeling accuracy, the entire heat exchanger can be regarded as multiple heat transfer units connected in series, as Figure 12a presents. For the i-th heat transfer unit in the heat exchanger, its dynamic behavior can be described by using the corresponding dynamic heat current model shown in Figure 12b. Connecting models of all these units gives the heat current model of the entire heat exchanger, as Figure 12b shows.

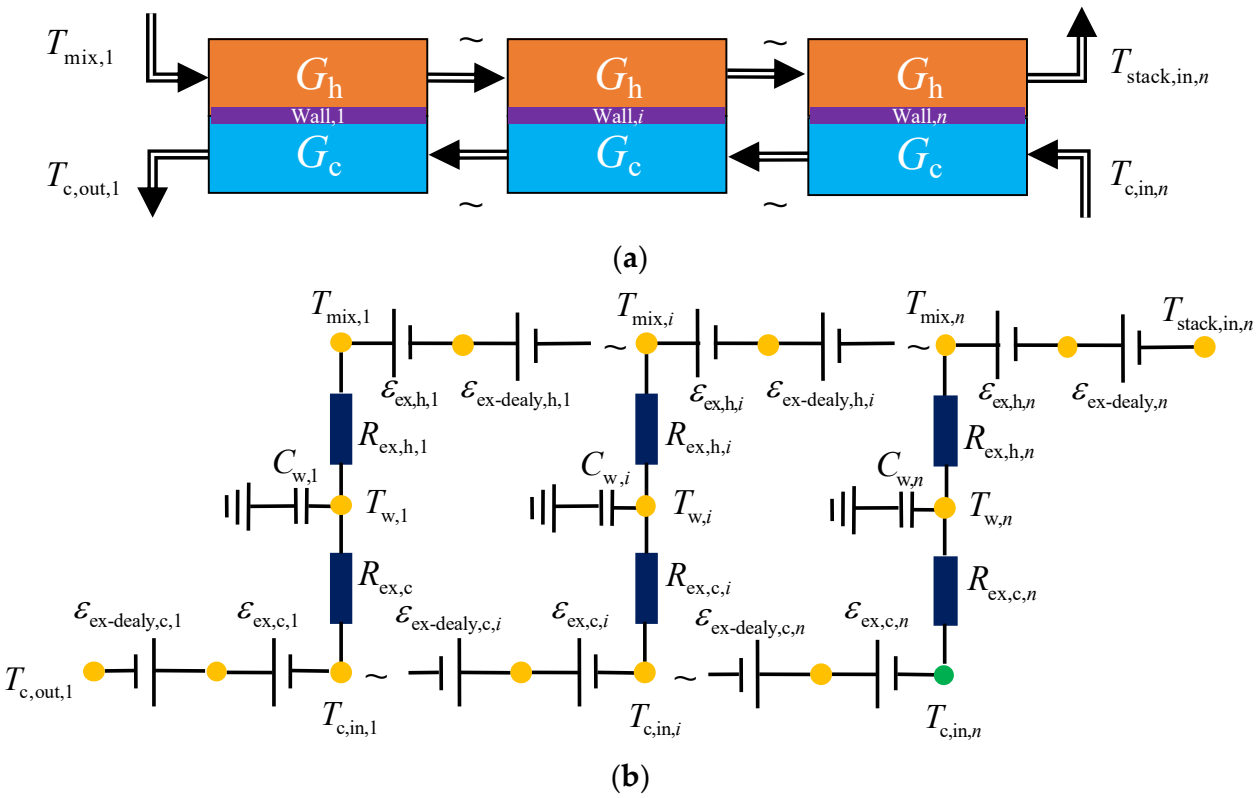


Figure 12. Dynamic heat current model of the segmented heat exchanger. (**a**) heat exchanger with multiple segments, (**b**) heat current model of the entire heat exchanger.

2.3.3. Overall Heat Current Model of the AWE System

After obtaining heat current models of all components, the overall heat current model of the AWE system can be constructed by connecting all component models according to node temperatures [31] as Figure 13 shows, where the heat exchanger is not divided for

clarity. The model represents the overall topology of the system and describes the heat transport processes inside. It has the form of electrical circuit and can be easily integrated with the electrochemical model, leading to the holistic and cross-scale analysis of the AWE system. Besides, it also builds a direct relationship between internal and external parameters, benefiting the overall system performance analysis.

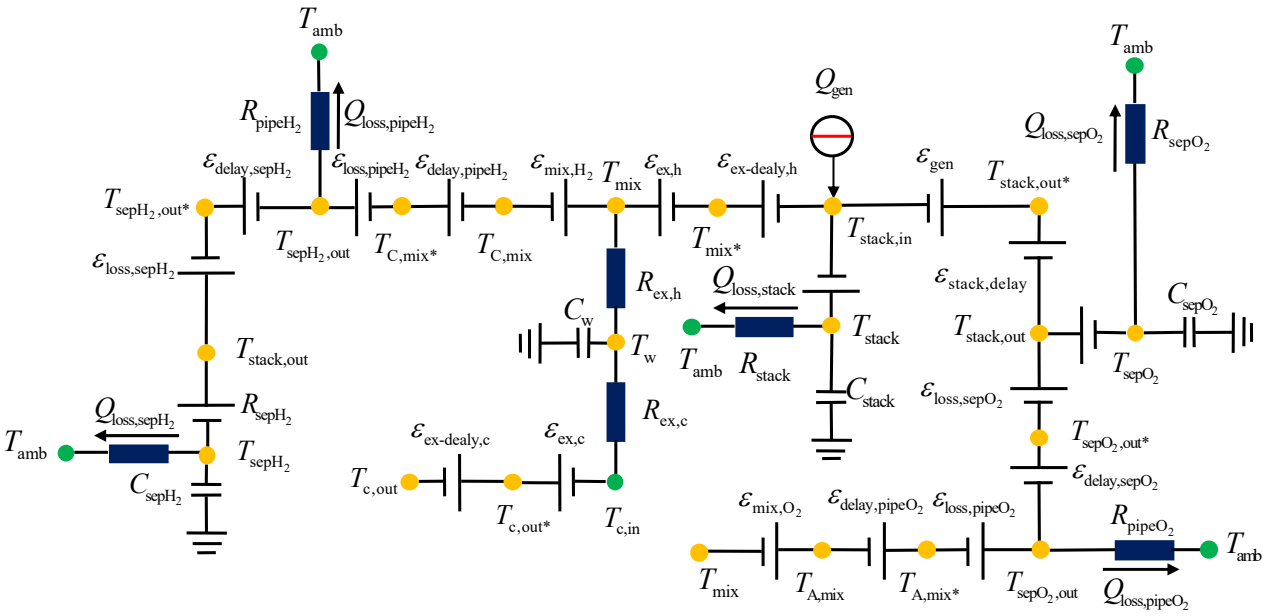


Figure 13. Overall heat current model of the AWE system.

2.4. System Energy Efficiency Evaluation

The Faraday efficiency and voltage efficiency are generally used to evaluate the efficiency of the AWE system. During the electrolysis process, hydrogen gas is produced at the cathode, and oxygen gas is produced at the anode. According to Faraday's law of electrolysis, the molar rate of hydrogen production and the mass flow rate are as follows [11]:

$$\dot{n}_{H_2} = \eta_F \frac{I}{zF} n \tag{70}$$

$$\dot{m}_{H_2} = M_{H_2} \dot{n}_{H_2} \tag{71}$$

where M_{H_2} is the molar mass of hydrogen, and η_F is the Faraday efficiency [11]:

$$\eta_F = \frac{J^2}{f_1 + J^2} f_2 \tag{72}$$

$$f_1 = 2.5(T - 273.15) + 50 \tag{73}$$

$$f_2 = 1 - 6.25 \times 10^{-6}(T - 273.15) \tag{74}$$

where J is the current density. According to the chemical reaction equation for water electrolysis, the mass balance for each component is expressed as [14]:

$$\dot{n}_{H_2} = \dot{n}_{H_2O} = 2\dot{n}_{O_2} \tag{75}$$

The voltage efficiency η_U is defined as the reversible voltage divided by the cell voltage [14]:

$$\eta_U = \frac{U_{rev}}{U_{cell}} \tag{76}$$

3. Model Solution Algorithm and Validation

3.1. Model Solution Algorithm

After constructing the system model, the governing equations of the system are directly obtained. In the system performance analysis, the current or voltage are generally given as the boundary condition. Once the initial conditions and necessary parameters are given, the unknown variables such as potential and node temperatures can be calculated and updated with respect to the time. Due to the introduction of heat current models, the additional intermediate variables and iteration layers have been reduced to the greatest extent, which allows for the efficient system simulation.

3.2. Model Validation

The model validation requires validating both electrochemical and heat current models. The heat current model has been proven accurate and effective in many studies, including the cases with electrochemical components [20,21]. Therefore, only the electrochemical model is validated here.

The validation of the electrochemical model is realized by comparing it against the experimental data collected from the HRI stack [25,32]. The HRI stack is assumed to be isothermal and operates at atmospheric pressure, and its parameters are shown in Table 2.

Table 2. System structure and operating parameters [25,32].

Parameters [Unit]	Value
Electrolyte concentration (w) [1]	0.3
Number of electrolysis cells (n)	24
Electrode thickness (δ_a, δ_c) [m]	0.2×10^{-3}
Electrode area (S_a, S_c) [m^2]	0.03
Diaphragm thickness (δ_m) [m]	0.5×10^{-3}
Diaphragm area (S_m) [m^2]	0.03
Electrode diaphragm spacing (d_{am}, d_{cm}) [m]	1.25×10^{-3}
Diaphragm tortuosity (τ_m) [1]	2.18
Diaphragm porosity (p_m) [1]	0.42

Solving the electrochemical model built in Section 2 gives the current-voltage polarization curve, with the corresponding experimental temperatures of 23 °C, 40 °C, and 45 °C substituted into the model, which is compared against the experimental data in Figure 14. It is found that the simulation results of the current-voltage polarization curve are highly consistent with the experimental data. The maximum relative error was less than 0.5%, and the average relative error was less than 0.3%. Therefore, the electrochemical model as well as the entire AWE model are validated.

The AWE system model is further validated by considering a steady-state case. In this case, the reference temperature and pressure are set to 25 °C and 1 bar, respectively. The cooling water flow rate is automatically regulated by a PID controller, and the electrolyte flow rate is set to 1.2 kg s^{-1}. The other parameters used in calculation are presented in Table 3.

In the simulation, the current increases from 2000 to 3500 and 4000 A, the cooling water flow rate is fixed to 0.3 kg s^{-1}, and the dynamic model of the AWE system is used to resolve the transient behavior of the system. The inlet and outlet temperatures of the stack gradually reaches the corresponding steady-state values after the transient relaxation process. When the current steps from 2000 A to 3500 A, the inlet temperature increases from 47.3 °C to 65.2 °C, and the outlet temperature rises from 57.4 °C to 83.1 °C. When the current steps from 2000 A to 4000 A, the inlet temperature increases from 47.3 °C to 70 °C, and the outlet temperature rises from 57.4 °C to 91 °C. The final values of the two temperatures are compared with the values directly obtained from the steady-state model [29], as Figure 15 shows. The comparison presents that the results are consistent

when the system reaches steady state, further implying the accuracy of the dynamic AWE system model.

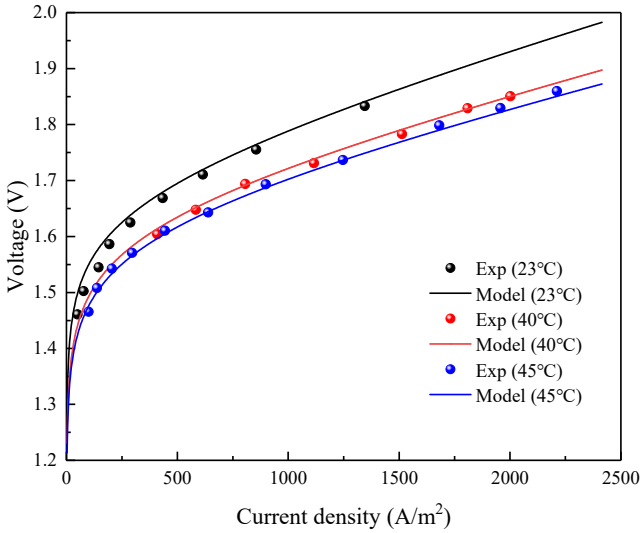


Figure 14. Comparison of polarization curves of the HRI stack.

Table 3. System structure and operating parameters.

Related Parameters [Unit]	Value
Electrolyte concentration w [1]	0.32
Specific heat capacity of electrolyte $c_{p,\mathrm{lye}}$ [J kg^{-1} K^{-1}]	3100
Ambient temperature T_{amb} [K]	298.15
Number of electrolysis cells n	80 (40 in series)
Electrode thickness δ_{a}, δ_{c} [m]	0.2×10^{-3}
Electrode area S_{a}, S_{c} [m^2]	0.42
Diaphragm thickness δ_{m} [m]	0.5×10^{-3}
Diaphragm area S_{m} [m^2]	0.42
Electrode and diaphragm spacing d_{am}, d_{cm} [m]	2×10^{-3}
Diaphragm tortuosity τ_{m} [1]	5.2
Diaphragm porosity p_{m} [1]	0.59
stack thermal resistance R_{stack} [K W^{-1}]	0.025
Gas-liquid separator thermal resistance R_{sep} [K W^{-1}]	0.04
Stack heat capacity C_{stack} [J K^{-1}]	400,000
Hydrogen/oxygen liquid separator heat capacity C_{sep} [J K^{-1}]	450,000
Heat capacity of the heat exchanger wall C_{w} [J K^{-1}]	18,940
Specific heat capacity of hydrogen $c_{\mathrm{H_2}}$ [J kg^{-1} K^{-1}]	$c_{\mathrm{H_2}} = \frac{(27.28+0.00326T+50000/T^2)}{0.002}$
Specific heat capacity of oxygen $c_{\mathrm{O_2}}$ [J kg^{-1} K^{-1}]	$c_{\mathrm{O_2}} = \frac{(29.96+0.00418T-167000/T^2)}{0.032}$
Stack delay time $\Delta t_{\mathrm{stack}}$ [s]	60
Heat exchanger cold/hot fluid delay time Δt_{ex} [s]	40
Gas-liquid separator delay time Δt_{sep} [s]	30
Hydrogen/oxygen side tubing diameter d_{pipe} [m]	0.02
Heat transfer coefficient of hydrogen/oxygen side lines K_{pipe} [W m^{-2} K^{-1}]	20
Hydrogen/oxygen side line length L_{pipe} [m]	3
KA_{h} [W K^{-1}]	8000
KA_{c} [W K^{-1}]	8000
U_{th} [V]	1.48
PID parameter kp	0.0055
PID parameter ki	0.00006
PID parameter kd	0

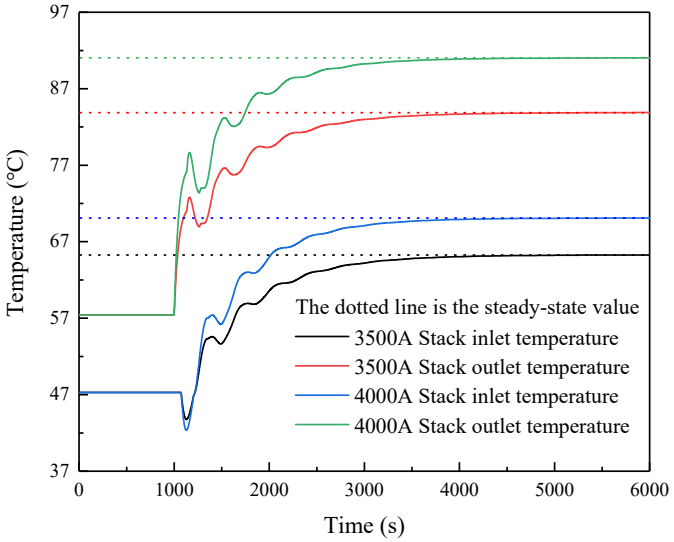


Figure 15. Comparison of the results of the dynamic temperature model of the inlet and outlet of the stack and the steady-state model.

4. Dynamic Simulation and Performance Analysis of the AWE System

4.1. Multi-Time Scale Dynamic Behavior of the AWE System

The constructed holistic dynamic model of the AWE system resolves both second-level electrical response and minute-level thermal response. Here, the dynamic operation protocol of the AWE system shown in Figure 1 is first considered, and the system parameters are given in Table 3. During the operation, the current varies 500 A for every two hours starting from 3000 A at 1 h, and the average stack temperature obtained from the simulation is given in Figure 16. It is found that the increase of current leads to the higher heat generation, and hence the stack temperature increases. Meanwhile, the cooling water flow rate is adjusted by the PID controller automatically to maintain the average temperature at around 70 °C. However, due to the delay in the heat transport process, temperature fluctuations occur during the adjustment. The temperature fluctuation is around 2.6 °C, and it takes approximately 40 min to return to the set point.

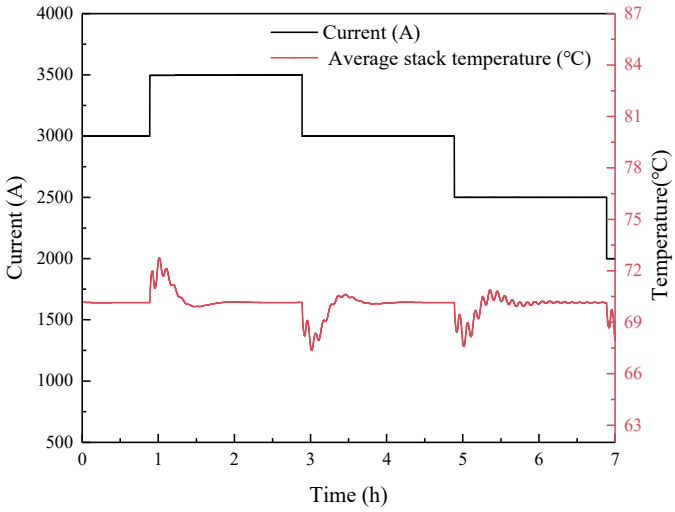


Figure 16. Average stack temperature variation with the current variation.

Figure 17 presents the variation of voltage and voltage efficiency over time under the same operating condition during the first step. Due to the interaction between the second-level response of voltage and the minute-level response of temperature, when the current varies, the voltage initially experiences a step change and then oscillates, as it is

also influenced by temperature before reaching the steady state. Its maximum fluctuation value is approximately 0.025 V, when the temperature stabilizes, the voltage also stabilizes. The trend of voltage efficiency is opposite to that of voltage. This is because the voltage efficiency is defined as the reversible voltage divided by the total voltage. As current increases, the total voltage rises, while the reversible voltage remains relatively constant with respect to the current, resulting in a decrease in voltage efficiency. However, an increase in temperature can improve the efficiency of the electrolysis reaction by accelerating reaction rates, enhancing electrolyte conductivity, reducing overpotential, and promoting gas diffusion. Therefore, fluctuations in temperature can lead to fluctuations in voltage efficiency as well. In this case, the maximum fluctuation in efficiency is less than 1%.

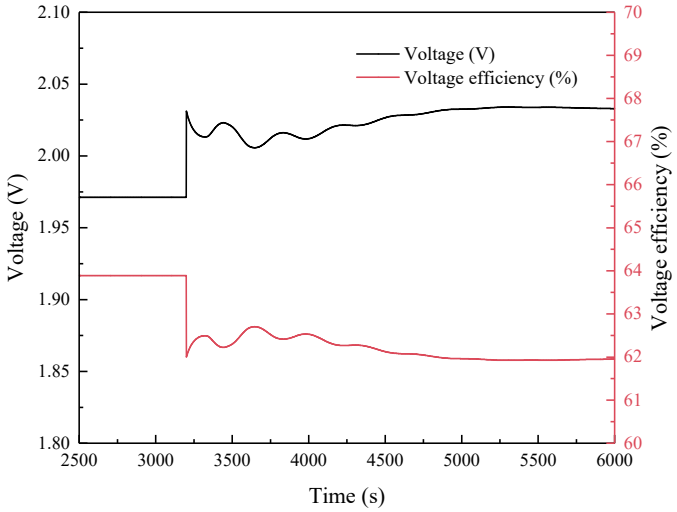


Figure 17. Voltage and voltage efficiency over time in the case of current steps.

4.2. Hydrogen Production Rate Variation and Temperature Controlling in the Dynamic Operation

The hydrogen production rate and Faraday efficiency of the AWE system is crucial in practice, especially when the input current is unstable, such as wind and photovoltaic power. Here, the hydrogen production rate and Faraday efficiency of the AWE system in Figure 1 are calculated with the input current shown in Figure 18. This current is based on the data from Oikonomidis et al. [33] and has the typical fluctuation mode of wind power. The other parameters are given in Table 3.

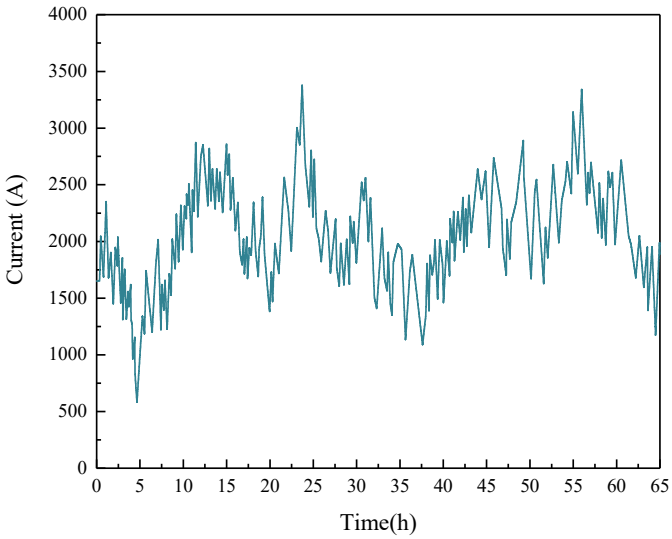


Figure 18. Input current in evaluation of hydrogen production rate and Faraday efficiency.

Under the combined influence of current and temperature, the curve of hydrogen production rate over time is shown in Figure 19, and Faraday efficiency variation during the operation is shown in Figure 20. Faraday efficiency is the ratio of the actual yield of the target product to the theoretical yield under a certain amount of electric charge, or the ratio of the electric charge used to produce the target product to the theoretically consumed electric charge. It is used to determine whether any side reactions occur during the process and serve as the performance indicator of the system. The hydrogen production rate is directly proportional to the current and is significantly influenced by Faraday efficiency at low current densities. Undesirable side reactions may occur on the electrode, consuming part of the current and leading to a decrease in Faraday efficiency. At low current density, the total current is relatively small, and a significant portion is consumed by side reactions. However, when the current is larger, the proportion of current consumed by side reactions is relatively less noticeable.

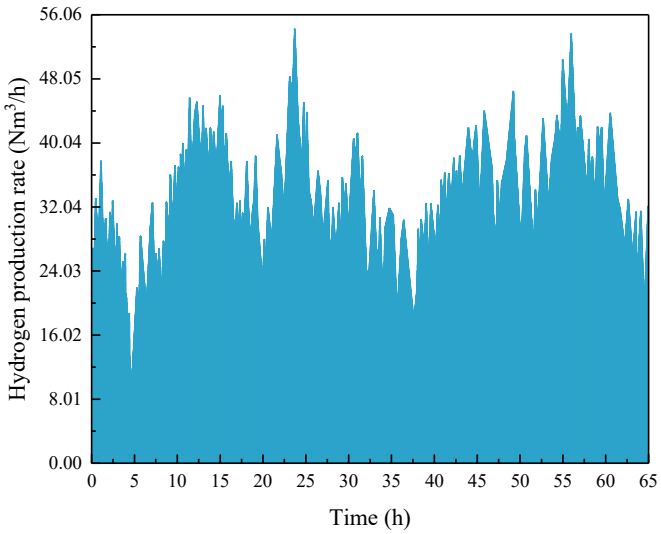


Figure 19. Hydrogen production rate over time.

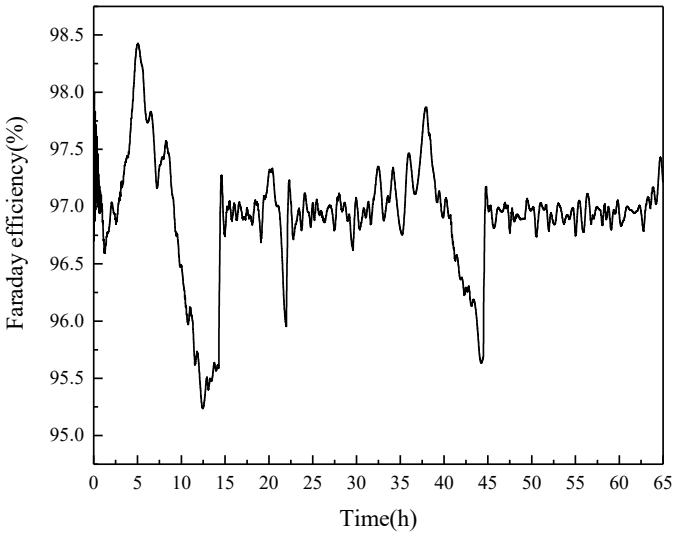


Figure 20. Faraday efficiency over time.

Under dynamic operating conditions, the variations of load may have disturbances on the stack temperature. When the load undergoes a sudden change, it can lead to a temperature overshoot, which may exceed the safety temperature limit and cause damage to the stack, reducing its lifespan. Therefore, the effective thermal management of the stack

is crucial. Here, the stack power, average temperature, and the cooling water flow rate between 15 and 40 h in the case above are shown in Figure 21. It is found that the average stack temperature fluctuates around 70 °C, which is attributed to the automatic adjustment of the cooling water flow rate. In the low-load region, the cooling water flow rate is limited to the minimum opening of the cooling water valve, which is 0.1 kg s^{-1}. In the high-load region, increasing the cooling water flow rate helps reduce the average stack temperature, with a maximum temperature overshoot of around 10 °C. For large-scale AWE systems, the high-load region is wider, in most cases, the power that the stack can flexibly load ranges from 10% to 110% of its rated power, Occasional short-term overshoot does not affect the lifespan of the stack; however, long-term occurrences of such conditions should be avoided. Increasing the thermal capacity of the stack can prevent temperature overshoot in the short term. However, from a cost and design perspective, minimizing the stack material usage is preferable to reduce costs and lower its weight.

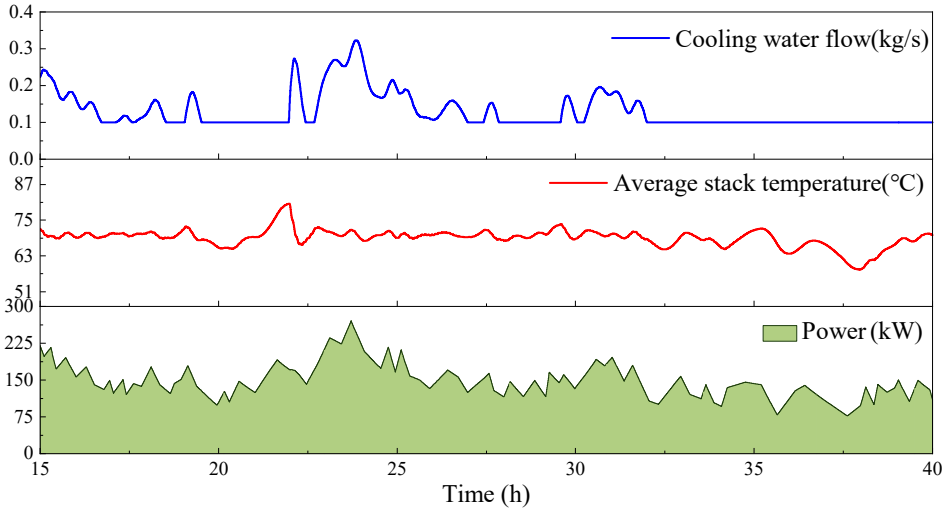


Figure 21. Cooling water flow, temperature, and power of the stack for 15–40 h.

We note that this study focuses on modeling and does not delve into the controller design. In future studies, the reduction of temperature overshoot by designing more advanced controllers would be considered. Such as current feedforward control or model predictive control. Once the performance of a single stack is stabilized, scalability in large-scale applications can be achieved by connecting multiple stacks in series or parallel. This approach can be used to support renewable energy integration or large-scale hydrogen production.

5. Conclusions

The dynamic modeling and analysis of AWE systems are crucial to enhance their energy efficiency under the fluctuating input. This work establishes a holistic model of the AWE system and realizes the unified modeling and the analysis of the system. The major conclusions are as follows:

(1) An equivalent circuit model for electrochemistry and a heat current model for the thermal management system are first established. The two models have the same form and are coupled through the energy conservation relation, forming the holistic model of the AWE system, which can be solved by using a single solver.

(2) The holistic model is verified by comparing the current-voltage polarization curve with experimental data from the HRI stack test. The maximum and average relative errors are less than 0.5% and 0.3%, respectively, showing the high accuracy of the proposed model. Besides, the system model is further validated by comparing with the steady-state model during the relaxation process.

(3) Due to the different response characteristics of voltage and temperature, there is a delay in temperature regulation. This delay causes voltage oscillations following

current fluctuations before eventually reaching a steady state as temperature stabilizes. Due to the rapid response of the voltage, the temperature will suddenly rise by about 2 °C when there is a current step of 500 A, and then return to the set temperature point. Because of this phenomenon, the trend of voltage efficiency is opposite to that of voltage.

(4) The hydrogen production rate is positively correlated with the current. When the AWE system operates under high power conditions, The Faraday efficiency is stable and close to 1. Under dynamic operating conditions, sudden load changes can lead to temperature overshoot, potentially exceeding the safety limit and damaging the stack, thus reducing its operational lifespan. In large-scale AWE systems, temperature overshoot is more common in broader high-load regions. Future work could focus on minimizing this overshoot through the design of more advanced controllers.

Author Contributions: Conceptualization, T.Z. and Y.-C.J.; Methodology, Y.-C.J.; Software, Y.-C.J.; Validation, T.Z. and Y.-C.J.; Formal analysis, S.-M.D.; Investigation, X.-L.W.; Resources, L.S.; Data curation, B.Y.; Writing—original draft preparation, Y.-C.J. and Z.L.; Writing—review and editing, T.Z.; Visualization, Y.-C.J.; Supervision, T.Z.; Project administration, T.Z.; Funding acquisition, T.Z. and S.-M.D. All authors have read and agreed to the published version of the manuscript.

Funding: This work was supported by Science and Technology Project of State Grid Corporation of China (SGNX0000DKJS2200808).

Data Availability Statement: Data can be made available upon reasonable request.

Conflicts of Interest: Author S.-M. D was employed by the company National Power Dispatch and Control Center, SGCC. Authors X.-L.W., L.S. and B.Y. were employed by the company State Grid Ningxia Electric Power Co., Ltd. The remaining authors declare that the research was conducted in the absence of any commercial or financial relationships that could be construed as a potential conflict of interest.

References

1. Emam, A.S.; Hamdan, M.O.; Abu-Nabah, B.A.; Elnajjar, E. A review on recent trends, challenges, and innovations in alkaline water electrolysis. *Int. J. Hydrogen Energy* **2024**, *64*, 599–625. [CrossRef]
2. Sebbahi, S.; Assila, A.; Belghiti, A.A.; Laasri, S.; Kaya, S.; Rachidi, S.; Hajjaji, A. A comprehensive review of recent advances in alkaline water electrolysis for hydrogen production. *Int. J. Hydrogen Energy* **2024**, *82*, 583–599. [CrossRef]
3. Huang, C.; Zong, Y.; You, S.; Træholt, C. Economic model predictive control for multi-energy system considering hydrogen-thermal-electric dynamics and waste heat recovery of MW-level alkaline electrolyzer. *Energy Convers. Manag.* **2022**, *265*, 115697. [CrossRef]
4. Diéguez, P.M.; Ursúa, A.; Sanchis, P.; Sopena, C.; Guelbenzu, E.; Gandía, L.M. Thermal performance of a commercial alkaline water electrolyzer: Experimental study and mathematical modeling. *Int. J. Hydrogen Energy* **2008**, *33*, 7338–7354. [CrossRef]
5. Vidales, A.G.; Millan, N.C.; Bock, C. Modeling of anion exchange membrane water electrolyzers: The influence of operating parameters. *Chem. Eng. Res. Des.* **2023**, *194*, 636–648. [CrossRef]
6. David, M.; Ocampo-Martínez, C.; Sánchez-Peña, R. Advances in alkaline water electrolyzers: A review. *J. Energy Storage* **2019**, *23*, 392–403. [CrossRef]
7. Brauns, J.; Turek, T. Experimental evaluation of dynamic operating concepts for alkaline water electrolyzers powered by renewable energy. *Electrochim. Acta* **2022**, *404*, 139715. [CrossRef]
8. Yang, M.; Hu, S.; Yang, F.; Fang, C.; Deng, W.; Lu, Z.; Bu, Y. Theoretical analysis on energy saving of cold energy utilization system for a liquid hydrogen heavy-duty truck. *Appl. Therm. Eng.* **2023**, *219*, 119509. [CrossRef]
9. Qi, R.; Li, J.; Lin, J.; Song, Y.; Wang, J.; Cui, Q.; Qiu, Y.; Tang, M.; Wang, J. Thermal modeling and controller design of an alkaline electrolysis system under dynamic operating conditions. *Appl. Energy* **2023**, *332*, 120551. [CrossRef]
10. Jaeseung, L.; Afroz, A.; Hyunchul, J. Multidimensional and transient modeling of an alkaline water electrolysis cell. *Int. J. Hydrogen Energy* **2020**, *46*, 13678–13690.
11. Øystein, U. Modeling of advanced alkaline electrolyzers: A system simulation approach. *Int. J. Hydrogen Energy* **2003**, *28*, 21–33.
12. Jang, D.; Cho, H.S.; Kang, S. Numerical modeling and analysis of the effect of pressure on the performance of an alkaline water electrolysis system. *Appl. Energy* **2021**, *287*, 116554. [CrossRef]
13. Sakas, G.; Ibáñez-Rioja, A.; Ruuskanen, V.; Kosonen, A.; Ahola, J.; Bergmann, O. Dynamic energy and mass balance model for an industrial alkaline water electrolyzer plant process. *Int. J. Hydrogen Energy* **2022**, *47*, 4328–4345. [CrossRef]
14. Ding, S.; Guo, B.; Hu, S.; Tian, Z.; Gu, J.; Zhang, T.; Yang, F.; Ouyang, M. Experimental and modeling study on energy flow of 250 kW alkaline water electrolysis system under steady state conditions and cold start process. *Fuel* **2023**, *350*, 128799. [CrossRef]

15. Ursúa, A.; Sanchis, P. Static–dynamic modelling of the electrical behaviour of a commercial advanced alkaline water electrolyser. *Int. J. Hydrogen Energy* **2012**, *37*, 18598–18614. [CrossRef]
16. Chen, Q.; Hao, J.H.; Zhao, T. An alternative energy flow model for analysis and optimization of heat transfer systems. *Int. J. Heat Mass Transf.* **2017**, *108*, 712–720. [CrossRef]
17. Hao, J.; Chen, Q.; Li, X.; Zhao, T. A correction factor-based general thermal resistance formula for heat exchanger design and performance analysis. *J. Therm. Sci.* **2021**, *30*, 892–901. [CrossRef]
18. Xin, Y.L.; Zhao, T.; Chen, X.; He, K.L.; Ma, H.; Chen, Q. Heat current method-based real-time coordination of power and heat generation of multi-CHP units with flexibility retrofits. *Energy* **2022**, *252*, 124018. [CrossRef]
19. He, K.L.; Zhao, T.; Ma, H.; Chen, Q. Optimal operation of integrated power and thermal systems for flexibility improvement based on evaluation and utilization of heat storage in district heating systems. *Energy* **2023**, *274*, 127421. [CrossRef]
20. Hao, J.; Hao, T.; Lu, Z.; Hong, F.; Du, X.; Ge, Z. Cross-scale modeling and optimization analysis of the solid oxide fuel cell cogeneration system based on the heat current method. *Energy Convers. Manag.* **2023**, *280*, 116828. [CrossRef]
21. Liang, Z.; Zhao, T.; Ma, H.; Chen, Q.; Wang, S. An isomorphic multi-energy circuit analysis method for multi-stack SOFC systems considering nonlinear electrochemical reaction and gas transport. *Appl. Energy* **2025**, *377*, 124503. [CrossRef]
22. He, K.L.; Chen, Q.; Liu, Y.T.; Hao, J.-H.; Wang, Y.-F.; Yuan, Y. A transient heat current model for dynamic performance analysis and optimal control of heat transfer system. *Int. J. Heat Mass Transf.* **2019**, *145*, 118767. [CrossRef]
23. Olivier, P.; Bourasseau, C.; Bouamama, P.B. Low-temperature electrolysis system modelling: A review. *Renew. Sustain. Energy Rev.* **2017**, *78*, 280–300. [CrossRef]
24. Hu, S.; Guo, B.; Ding, S.; Yang, F.; Dang, J.; Liu, B.; Gu, J.; Ma, J.; Ouyang, M. A comprehensive review of alkaline water electrolysis mathematical modeling. *Appl. Energy* **2022**, *327*, 120099. [CrossRef]
25. Abdin, Z.; Webb, C.; Gray, M.E. Modelling and simulation of an alkaline electrolyser cell. *Energy* **2017**, *138*, 316–331. [CrossRef]
26. Gilliam, R.J.; Graydon, J.W.; Kirk, D.W.; Thorpe, S.J. A review of specific conductivities of potassium hydroxide solutions for various concentrations and temperatures. *Int. J. Hydrogen Energy* **2007**, *32*, 359–364. [CrossRef]
27. Deng, X.; Yang, F.; Li, Y.; Dang, J.; Ouyang, M. Quantitative study on gas evolution effects under large current density in zero-gap alkaline water electrolyzers. *J. Power Sources* **2023**, *555*, 232378. [CrossRef]
28. Rodríguez, J.; Palmas, S.; Sánchez-Molina, M.; Amores, E.; Mais, L.; Campana, R. Simple and precise approach for determination of Ohmic contribution of diaphragms in alkaline water electrolysis. *Membranes* **2019**, *9*, 129. [CrossRef]
29. Jiang, Y.; Wu, J.; He, K.; Zhang, Y.; Chen, Q.; Zhang, M.; Zhao, T.; Liu, Y. Performance Analysis of Alkaline Water Electrolysis System Based on Heat Current Modeling Method. In Proceedings of the 2024 IEEE 2nd International Conference on Power Science and Technology (ICPST), Dali, China, 9–11 May 2024; IEEE: Piscataway, NJ, USA, 2024; pp. 1785–1794.
30. He, K.L.; Chen, Q.; Ma, H.; Zhao, T.; Hao, J.H. An isomorphic multi-energy flow modeling for integrated power and thermal system considering nonlinear heat transfer constraint. *Energy* **2020**, *211*, 119003. [CrossRef]
31. Zhao, T.; Chen, X.; He, K.L.; Chen, Q. A standardized modeling strategy for heat current method-based analysis and simulation of thermal systems. *Energy* **2021**, *217*, 119403. [CrossRef]
32. Henao, C.; Agbossou, K.; Hammoudi, M.; Dubé, Y.; Cardenas, A. Simulation tool based on a physics model and an electrical analogy for an alkaline electrolyser. *J. Power Sources* **2014**, *250*, 58–67. [CrossRef]
33. Oikonomidis, S.; Ramdin, M.; Moultos, O.A.; Bos, A.; Vlugt, T.J.; Rahbari, A. Transient modelling of a multi-cell alkaline electrolyzer for gas crossover and safe system operation. *Int. J. Hydrogen Energy* **2023**, *48*, 34210–34228. [CrossRef]

Disclaimer/Publisher's Note: The statements, opinions and data contained in all publications are solely those of the individual author(s) and contributor(s) and not of MDPI and/or the editor(s). MDPI and/or the editor(s) disclaim responsibility for any injury to people or property resulting from any ideas, methods, instructions or products referred to in the content.